Synthesis of free-standing carbon nanotube buckypaper films decorated with Fe_3O_4 nanoparticles and polyaniline as highly effective electromagnetic shielding materials

Hu Yunping[1,2,†], Gong Daixuan[2,†], Qu Meijie[2], Tang Ping[2], Bin Yuezhen[2,*]

(1. *The* 404 *Company Limited*, *China National Nuclear Corporation*, *Jiayuguan* 735100, *China*;
2. *Department of Polymer Science and Engineering*, *College of Chemical Engineering*, *Dalian University of Technology*, *Dalian* 116024, *China*)

Abstract: A balance between electrical and magnetic properties is critical for electromagnetic shielding materials to achieve excellent electromagnetic interference (EMI) shielding and attenuation effectiveness across a broad frequency range. We have prepared free-standing buckypaper films (BPFP) decorated with Fe_3O_4 particles and polyaniline (PANI) by a simple two-step method to meet this requirement. First, buckypaper films decorated with Fe_3O_4 (BPF) were synthesized by the coprecipitation of Fe^{2+}/Fe^{3+} ions on buckypaper (BP) which was then coated with a polyaniline layer by the in situ polymerization of aniline monomers. Magnetic characterization revealed that the BPF and BPFP films had saturation magnetization (M_s) values of 14.3 emu g^{-1} and 13.0 emu g^{-1}, respectively, confirming retention of the magnetic phase. The addition of Fe_3O_4 nanoparticles and polyaniline to BP (30 μm) increased both the magnetic and dielectric losses due to the increased interfacial polarizations and anisotropy energy. 41 μm-thick BPF and BPFP films had an absorption-dominated shielding effectiveness of 35.1 dB and 36.4 dB, respectively, across the 5.85-18 GHz frequency band. These values are respectively 12.9% and 17.0% greater than that of pristine BP, highlighting the positive effect of Fe_3O_4-PANI heterostructures on electromagnetic wave dissipation. These films also had the tensile strength, flexibility, and lightness of BP, demonstrating exceptional promise for next-generation electromagnetic shielding materials.

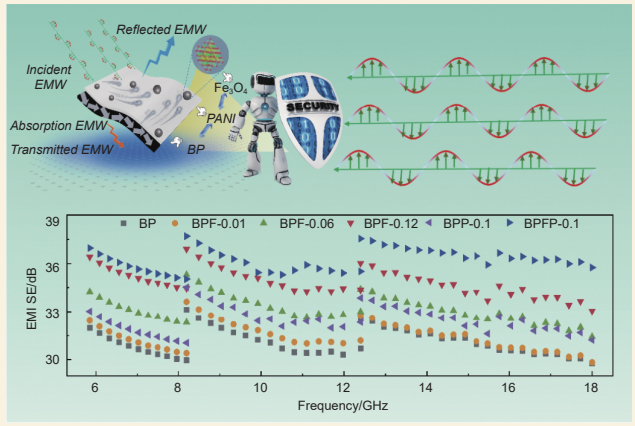

Key words: Buckypaper; Fe_3O_4 nanoparticles; In situ polymerization; Polyaniline; Electromagnetic interference

1 Introduction

With the ongoing miniaturization and integration of modern electronic devices, there is an irreversible trend toward developing lightweight and thin shielding materials with high performance that includes broad-spectrum electromagnetic wave absorption[1−2]. The electromagnetic interference (EMI) shielding effectiveness (SE) demonstrates a positive correlation with the conductivity and thickness of the shielding materials[3−4]. More importantly, impedance matching and maximum attenuation at a specific thickness are related to the electrical and magnetic properties of the electromagnetic shielding materials. Electrical permittivity derived from the electric dipoles and magnetic permeability provided by the magnetic dipoles of the composites[5] should be in an optimal balance in order to achieve highly improved EMI shielding and attenuation performance.

Carbon nanotubes (CNTs), encompassing both multi-walled (MWCNTs) and single-walled (SWCNTs) variants, have emerged as a cornerstone of nanotechnology since Iijima's structural elucidation of MWCNTs in 1991[6]. CNTs exhibit extraordinary

Received: November 28, 2025
Revised: February 25, 2026
Accepted: February 26, 2026

electrical, thermal and mechanical properties, and excellent microwave absorbing properties, which meet the requirements of lightweight, broadband and high absorption efficiency for new electromagnetic shielding materials[7−12]. Although considerable efforts have been made toward the development of CNT-based composites for electromagnetic shielding purpose recently, these materials are non-magnetic and preferential to microwave energy absorption mostly attributed to their dielectric loss. Furthermore, the dielectric permittivity and magnetic permeability of CNTs are out of balance, which results in a bad impedance matching characteristic[13]. In order to compensate the magnetic loss and strengthen impedance matching, ingredients with magnetic and dielectric features were frequently used in the preparation of microwave absorbers[14−17]. Among all of the magnetic materials, Fe_3O_4 nanoparticles are highly favored[13,18−19] owing to their high saturation magnetization, low toxicity and good biocompatibility. In terms of dielectric materials, the applications of graphene[16,20], CNTs[15] and conducting polymers have demonstrated exceptional performance. In previous literature, the evaluation of microwave absorption properties of MWCNT/MnO_2[18], MWCNT/Fe_3O_4[21−22], and MWCNT/Fe_3O_4/polyaniline[15] was carried out using composites of these nanofillers for wax and resin. Although the thicknesses of these composites were increased, it was very difficult to attain a high EMI SE because of the inhomogeneously dispersed fillers in polymer matrix due to the intrinsic aggregation feature of small sized fillers[9]. As reported by Biswas et al., PC/PVDF with a 3% (mass fraction) MWCNT/MnO_2 filler content and a thickness of 0.9 mm showed a maximum SE of ~ 21 dB in the frequency range of 8-18 GHz, which was not efficient[18]. The comparable SE of composites using MWCNT/Fe_3O_4[21] and MWCNT/Fe_3O_4/polyaniline[15] as fillers was also achieved at larger thickness, which was too thick for compact electronic devices.

Large thickness and high stiffness are major disadvantages for carbon-based electromagnetic shielding composites prepared by mechanical blending. Buckypaper (BP) is a free-standing and conductive film formed by entangled CNTs, which has presented a great potential for the next generation electromagnetic shielding materials owing to its high flexibility and electrical conductivity. Kumar et al.[23] prepared a Pb-CNT-Cu nanocomposite BP by vacuum filtration. An SE of 35 dB could be achieved in the frequency range of 12-18 GHz at a composite film thickness of only 200 μm. The investigation of Chaudhary et al. revealed that mesocarbon microbeads (MCMB)/MWCNT composite paper showed an SE of 31 to 56 dB at a thickness 0.15–0.6 mm. Beyond that, Fe_3O_4/MCMB/MWCNT composite paper prepared by simply mixing exhibited an excellent EMI SE of 80 dB at 0.5 mm thickness[13]. The above reported composite films for EMI shielding purpose were mostly prepared by means of vacuum filtration of the dispersion mixture of all components[13,24−25] or dispersion mixture of synthesized composites[23], which was a very efficient and convenient process. However, the tensile strength of composite films from vacuum filtration was critically low in most cases, which poses a major challenge for their long-term use in EMI related fields. Although a high EMI performance was obtained, the above-mentioned literatures have largely overlooked the evaluation of these very important parameters, which made the wide application of the composite films ambiguous. To develop electromagnetic shielding materials with integrated lightweight, thin-profile and high performance, this study, based on the design concept of multi-mechanism synergistic shielding, constructed a ternary composite system consisting of magnetic Fe_3O_4 nanoparticles, conductive CNTs and PANI. It aims to synergistically enhance the EMI SE while ensuring favorable mechanical properties, providing a feasible strategy for the development of practical high-performance flexible electromagnetic shielding materials.

Herein, free-standing buckypaper films (BPFP) decorated with Fe_3O_4 and PANI were prepared by a straightforward technique to expand the scope of electromagnetic shielding materials (Fig. 1a-b). First, BP/Fe_3O_4 (BPF) composite films were synthesized by

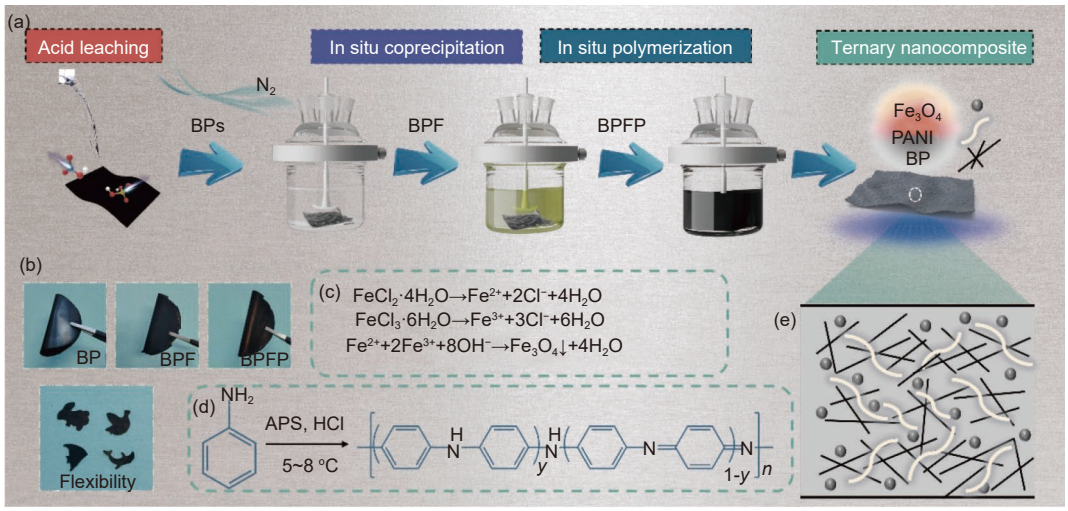

Fig. 1 (a) Schematic illustration of the preparation process for BPF, BPFP. (b) Bent state of BP, BPF and BPFP, and their animal shapes. (c) In situ coprecipitation of Fe_3O_4. (d) In situ polymerization of PANI. (e) Schematic of the microscopic morphology of BPFP

in situ coprecipitation of Fe^{2+} and Fe^{3+} on BP (Fig. 1c), and then decorated by in situ polymerization of aniline monomer to form PANI coating (Fig. 1d). Subsequently, the electromagnetic shielding performance of BP, binary and ternary BP composite films was investigated in detail in the frequency range of 5.85-18 GHz. BP/Fe_3O_4 and BP/Fe_3O_4/PANI composite films presented a significantly enhanced electromagnetic shielding performance due to the additional magnetic loss and dielectric loss caused by synergy of each component. Remarkably, these composite films maintained superior mechanical strength while retaining flexibility and lightness.

2 Experimental

2.1 Materials

MWCNTs with a diameter of 10–20 nm and a length of 10–30 μm were purchased from Chengdu Organic Chemicals Co., Ltd., China. Triton X-100, concentrated nitric acid (HNO_3), concentrated sulfuric acid (H_2SO_4), hydrochloric acid (HCl) and aqueous ammonia solution ($NH_3·H_2O$) were supplied by LiaoDong Chemical Reagent, China. Iron (Ⅲ) chloride hexahydrate ($FeCl_3·6H_2O$), iron(II) chloride tetrahydrate ($FeCl_2·4H_2O$), sodium dodecyl benzene sulfonate (SDBS), aniline (An) and ammonium peroxydisulphate ($(NH_4)_2S_2O_8$, APS) were purchased from Aladdin Chemical Reagent Corporation, China. Anhydrous ethanol was purchased from Tianjin Damao Chemical Reagent Factory, China. All chemicals were used as received except aniline. The aniline monomers were purified by vacuum distillation before use.

2.2 Preparation of buckypaper/Fe_3O_4 (BPF) composite film

The synthesis of BPF was carried out by in situ coprecipitation of Fe_3O_4 on CNT-based BP. Firstly, free-standing BP was prepared by the vacuum filtration method according to our previous work[26–27]. The thickness of the film was controlled by adjusting the volume of the CNT dispersion added during the vacuum filtration process. In a conventional vacuum filtration, MWCNT (20 mg) was subjected to ball milling for 0.5 h with a small amount of deionized water, then the obtained slurry was added into water containing 1% Triton X-100. Stable dispersion of MWCNTs is critical for the preparation of BP. With the aid of the non-ionic surfactant Triton X-100, CNTs can be uniformly dispersed in an aqueous solution, thus forming a stable dispersion. After the sonication of 0.5 h, the uniform dispersion was filtered through a cellulose membrane with the average pore size of 0.45 μm. Free-standing BP was obtained after the cellulose membrane filter was dissolved. Following this step, BP was immersed in a mixed concentrated acid solution (HNO_3 : H_2SO_4=1 : 3, v : v) to introduce carboxyl groups on the surface of MWCNTs, fol-

lowed by washing and drying.

300 mL deionized water was charged with a glass open reactor, from which oxygen was removed by vacuuming and filling nitrogen repeatedly. The as-prepared BP was attached to the reactor liner, followed by adding $FeCl_2·4H_2O$ (0.0131 mol/L) and $FeCl_3·6H_2O$ (0.0229 mol/L) with a molar ratio of 1∶1.75 under nitrogen atmosphere. Following 5 h of continuous mechanical agitation, an aqueous SDBS solution was introduced dropwise into the reactor under vigorous agitation (500 r/min) at 30 °C over a 1-hour period. Then $NH_3·H_2O$ (25%, mass fraction) was introduced dropwise into the reactor to adjust and maintain the pH = 11, inducing the heterogeneous nucleation of Fe_3O_4 nanoparticles on the BP substrate. After another 1 h stirring, the temperature was raised to 80 °C and aged for 2 h in order to promote the completeness of the growth of the Fe_3O_4 crystal structure. Subsequently, BPF was harvested, washed with deionized water and ethanol, and dried at 60 °C under vacuum. The total concentration of Fe^{2+} and Fe^{3+} ($C_{iron\ ion}$) was 0.12 mol/L during precursor addition, then the obtained BPF was named BPF-0.12. The BPF samples prepared at feeding iron-ion concentrations of 0.01 and 0.06 mol/L were designated as BPF-0.01 and BPF-0.06, respectively (Table 1). For comparison, Fe_3O_4 nanoparticles were synthesized by an analogous procedure without deposition on the BP substrate, and corresponding samples designated as Fe_3O_4-0.01, Fe_3O_4-0.06, and Fe_3O_4-0.12 based on their feeding iron-ion concentrations.

Table 1 Denotation of BP, binary and ternary BP composite films

Sample	$C_{iron\ ion}$/(mol/L)	$C_{aniline}$/(mol/L)
BP	0	0
BPF-0.01	0.01	0
BPF-0.06	0.06	0
BPF-0.12	0.12	0
BPP-0.02	0	0.02
BPP-0.1	0	0.10
BPP-0.5	0	0.50
BPFP-0.1	0.12	0.10
BPFP-0.5	0.12	0.50

2.3 Preparation of buckypaper/Fe_3O_4/polyaniline (BPFP) ternary composite films

The above-mentioned BPFs were used to prepare ternary composite films in the next step. BPF-0.12 was attached to the reactor liner and immersed in a 250 mL aqueous solution of HCl (1 mol/L). Aniline (0.025 mol) was subsequently added at a temperature of 5-8 °C under a nitrogen atmosphere. After stirring for 3 h, an equal molar amount of APS dissolved in aqueous HCl solution (1 mol/L HCl) was added into the reactor. BPFP was obtained after an 8-hour reaction, and washed with HCl solution (0.1 mol/L), ethanol, and deionized water in sequence, then dried using a freeze dryer before further measurement. BP/polyaniline (BPP) composite films were also prepared in a similar way using BP as a substrate, and PANI was prepared without a substrate. The as-prepared BPP and BPFP were denoted as BPP-0.1 and BPFP-0.1, respectively, because the feeding PANI concentration was 0.1 mol/L. The BPPs and BPFPs obtained at other aniline concentrations were named similarly (Table 1). In this way, the binary BP/Fe_3O_4 and BP/PANI composite films, and ternary BP/Fe_3O_4/PANI composite films were prepared for further measurement.

2.4 Characterization

The morphology and crystalline structure of the Fe_3O_4 nanoparticles were examined by a transmission electron microscope (TEM, Tecnai F30, FEI, USA). Surface morphology of BP, BPFs, BPPs, and BPFPs was measured by a scanning electron microscope (FE-SEM, NOVA NanoSEM 450, FEI, USA) equipped with an energy dispersive spectroscopy (EDS). Raman spectroscopy (DXR Microscope, Thermo Fisher, USA) was also used to detect the compositions of BPF, BPP and BPFP composite films. The crystalline structure and crystallite sizes of Fe_3O_4 in the composite films were characterized by an X-ray diffractometer (XRD, MiniFlex 600, Rigaku, Japan) with Cu *Kα* radiation. The contents of Fe_3O_4 and PANI of the composite films were estimated using a thermo gravimetric analyzer (TGA, NETZSCH TG 209, Netzsch, Germany) at a heating rate of 10 °C/min in air environment. The magnetic properties of Fe_3O_4 nanoparticles and composite films were detected by a vibrating sample magnetometer (VSM, LakeShore-

7400S, USA) with a maximum applied field of 6000 Oe. The electrical conductivities of BP and BP composite films were recorded with a testing four-point probe resistivity measurement system (model RST-9, PROBES TECH, China).

The EMI shielding performance was characterized by a waveguide measurement system using a vector network analyzer (3656D, the 41st Institute of China Electronics Technology Group Corporation) in C-band (5.85-8 GHz), X-band (8-12.4 GHz) and Ku-band (12.4-18 GHz). The samples were cut into a rectangular shape to fit the chamber of the sample holder. The incident electromagnetic wave passing through a material undergoes 4 different processes: reflection, absorption, penetration and multiple reflection[28–29]. The EMI SE is defined as the sum of reflection loss (SE_R) and absorption loss (SE_A). The EMI SE, SE_R and SE_A values were calculated as described in our previous work[26–27]. More details about the calculation of EMI SE are described in the Supporting Information.

3 Results and discussion

3.1 Morphology of composite films

The surface morphology of the BPFs is shown in Fig. 2. As for BPF-0.01, which had the lowest Fe^{2+}/Fe^{3+} feeding concentration, lamellar Fe_3O_4 was deposited onto the CNT surface. With increasing $C_{iron\ ion}$, Fe_3O_4 existed mostly as grains for BPF-0.06 and BPF-0.12, which could also be demonstrated by TEM images (Fig. S1). The amount of Fe_3O_4 deposited in BPF-0.12 was higher compared with BPF-0.06 due to the higher Fe^{2+}/Fe^{3+} feeding concentration. As can be seen in the magnified SEM images of BPF-0.06 and BPF-0.12, Fe_3O_4 particles were aligned along the axial direction of the CNTs. Agglomeration occurred between Fe_3O_4 particles due to their nanoscale dimensions and magnetic properties. The size distribution of Fe_3O_4 particles was located in the range of 20-200 nm.

PANI was uniformly coated onto the surface of CNTs by in situ polymerization of aniline (Fig. S2). When the aniline concentration was between 0.1 and 0.5 mol/L, PANI displayed flower-like morphology

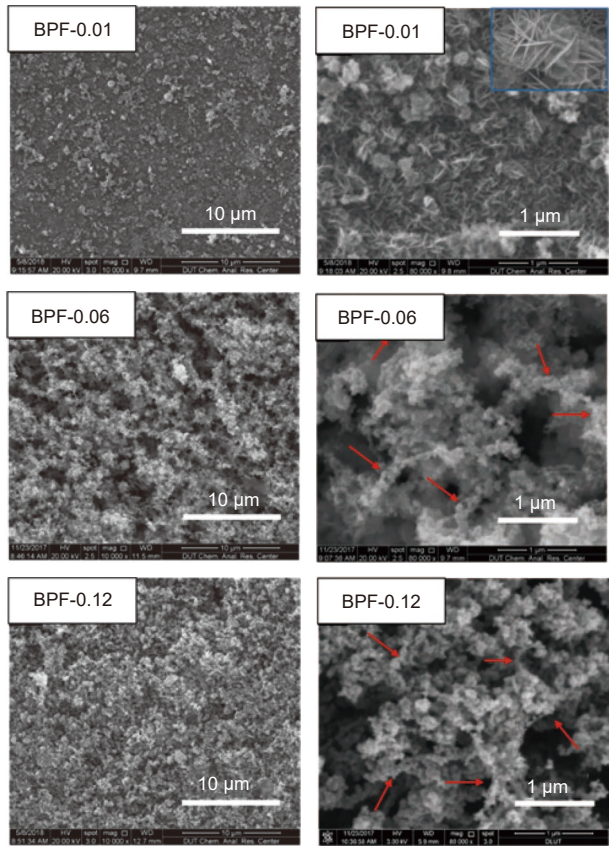

Fig. 2 SEM images of BPF prepared at different iron ion concentrations: BPF-0.01, BPF-0.06 and BPF-0.12

on the surface of CNTs, which could effectively increase the specific surface areas of the composites.

The SEM images showed that a remarkable morphology change took place on the external surface of Fe_3O_4 particles after the in situ polymerization of aniline (Fig. 3a and c). As shown in Fig. 3(b, d), the presence of Fe and O was mainly from Fe_3O_4, and Cl was derived from HCl-doped PANI. From Fig. 3a, the flower-like PANI was uniformly coated on the surface of Fe_3O_4 particles which greatly increased the specific surface area of the composite film. This would undoubtedly increase the attenuation of electromagnetic waves. In addition, the PANI networks acted as bridges between the CNTs and Fe_3O_4 particles, which enhanced the interaction between CNTs, Fe_3O_4 and PANI. As a result, the structural stability of BPFPs was strengthened simultaneously.

As shown in Fig. 3(a, c), the PANI flower-like structure of BPFP-0.1 was more well-developed, exhibiting a more significant increase in specific surface area compared to BPFP-0.5. Since the specific sur-

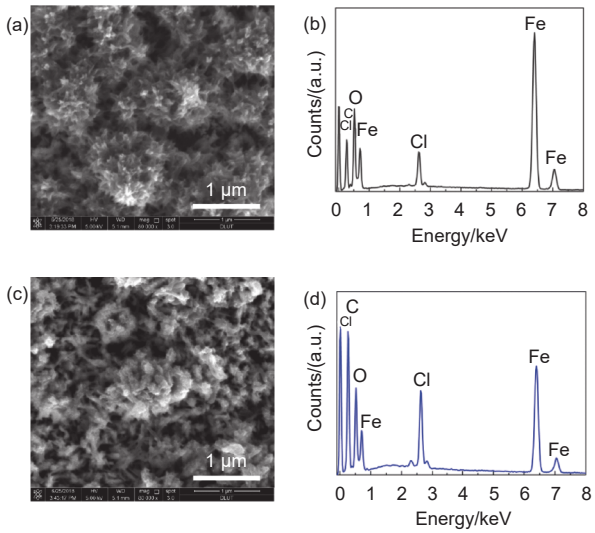

Fig. 3　SEM images and EDS of (a, b) BPFP-0.1 and (c, d) BPFP-0.5

face area is a key structural factor affecting the electromagnetic shielding performance of the composite, BPFP-0.1 was used as the key research object for subsequent studies.

3.2　Structural analysis of composite films

XRD patterns of Fe_3O_4, BP, BPPs, BPFs and BPFPs were collected from 2θ = 5° to 70° to investigate the crystallographic structure (Fig. 4a-b). The XRD profiles of Fe_3O_4 synthesized at $C_{iron\ ion}$ of 0.01, 0.06, 0.12, 0.25 and 0.50 mol/L are shown in Fig. S3. According to the standard XRD profiles (JCPDS No. 88-0315), diffraction peaks of Fe_3O_4, appearing at 2θ = 30.1°, 35.6°, 43.4°, 53.6°, 57.2° and 62.8°, were corresponding to (220), (311), (400), (422), (511) and (440) planes, respectively. The diffraction peak of BP at ca. 2θ = 26.2° was the (002) plane of CNTs. The characteristic diffraction peaks of Fe_3O_4 could be observed in the BP/Fe_3O_4 composite films, and the intensity of the diffraction peak increased with the increase of Fe^{2+}/Fe^{3+} feeding concentration. The interaction between the surface-loaded magnetic particles caused residual stress in MWCNTs. Therefore, the (002) diffraction peak of MWCNTs in the composite films shifted from 26.24° to 26.09°. At the same time, due to the constraint effects imposed by the MWCNT network, the crystal lattice of Fe_3O_4 in the composite films had a certain degree of distortion, which resulted in the shift of (311) diffraction from 30.02° to 30.53°. The crystallite sizes (D) of Fe_3O_4 were calculated using Scherrer's equation[30] based on the (311) plane, and were estimated to be ~ 20 nm for BPF-0.06 and BPF-0.12. The diffraction peaks of PANI were observed in the BPP film, indicating the presence of PANI on the surface of BP. The diffraction peaks of PANI were not obvious in BPFP due to the strong diffraction of Fe_3O_4 and BP. However, the shifting of the diffraction peak of (311) and (002) planes was also observed due to the interaction between MWCNTs, Fe_3O_4 and PANI.

The significant structural differences between BP, BPF, BPP and BPFP ternary composite films were reflected in the Raman spectra shown in Fig. 4(c-e). The spectra of BP displayed 2 characteristic peaks. The *D* band at ~ 1349 cm^{-1} was attributed to defects in the nanotube lattice, including the sp^3 hybridized carbon. The *G* band at ~ 1587 cm^{-1} was associated with tangential C—C bond stretching motions[31]. The strong peaks of *D* and *G* band were also observed in BPF. The shifting of *G* band has previously been used to reveal the interaction between nanoparticles and graphene or CNTs[32−33]. As shown in Fig. 4c, the *G* band of BPF-0.12 (1599 cm^{-1}) shifted to a higher wavenumber compared to BP (1587 cm^{-1}), indicating the charge transfer between carbon materials and Fe_3O_4 nanoparticles. In the case of BPF-0.06, the shifting was less (shift to1593 cm^{-1}) than that of BPF-0.12, due to the lower Fe_3O_4 concentration.

For ternary nanocomposite films (BPFPs) (Fig. 4e), there was no shift of the *G* band, but the *D* band shifted from 1349 to 1340 cm^{-1}, indicating a π-π interaction along with the charge transfer between PANI and CNTs. The band at 1406 cm^{-1} arose from the electronic absorption of free charge carriers. Furthermore, the peaks of BPFP at 1171 and 1613 cm^{-1} represented the C—H bending of the quinoid ring and the C—C stretching of the benzene ring. The $C—N^+$ stretching vibration, C—N stretching vibration, and N—H bending could also be observed at 1332, 1478 and 1485 cm^{-1}, respectively[16]. These peaks demonstrated the existence of doped PANI layer on BPFPs, and these were also observed in BPPs (Fig. 4d).

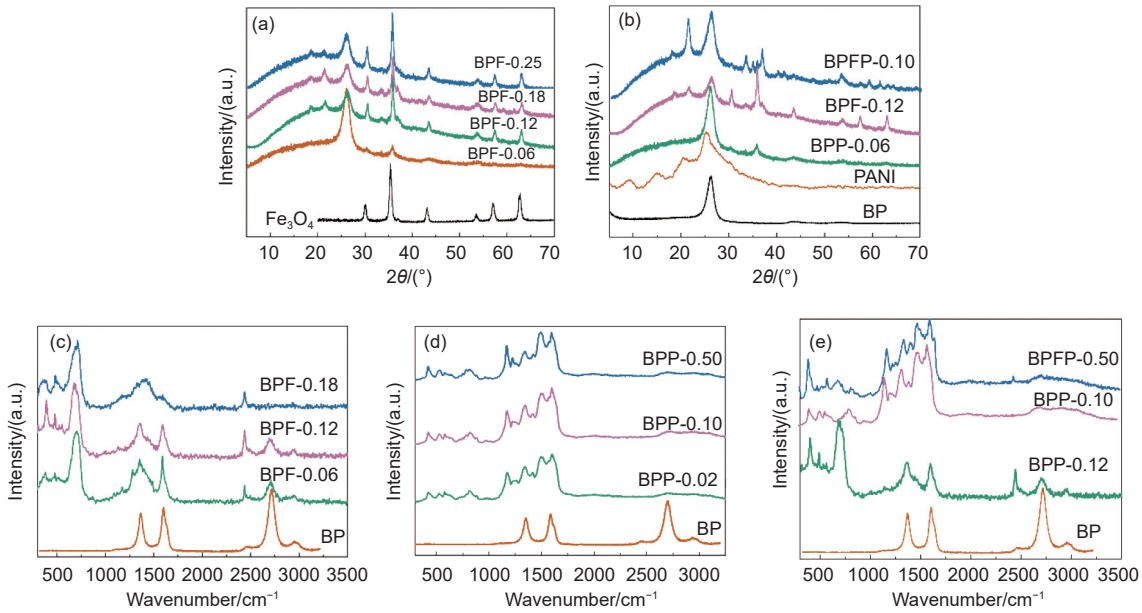

Fig. 4 XRD patterns of (a) Fe_3O_4, BP, BPF-0.06, BPF-0.12 and (b) PANI, BP, BPP-0.1, BPFP-0.1. Raman spectra of (c) Fe_3O_4, BP, BPF-0.06, BPF-0.12, (d) BP, BPP-0.02, BPP-0.1, BPP-0.5, and (e) BP, BPF-0.12, BPP-0.1, BPFP-0.1

As shown in Fig. 5a, the weight increase in Fe_3O_4 over a broad temperature range was caused by the oxidation of the Fe_3O_4 into Fe_2O_3. For BP, an obvious weight loss occurred at 470-630 °C due to the oxidation of the CNTs[34]. By contrast, BPF-0.06 and BPF-0.12 decomposed at a lower temperature range of 440-610 °C, due to the catalytic role of Fe_3O_4 in the oxidation of CNTs[35]. The residue weight of BPF-0.06 indicated that the weight fraction of Fe_3O_4 in BPF-0.06 was about 13.4%. The Fe_3O_4 content increased to 35.2% for BPF-0.12 with the increasing in $C_{iron\ ion}$. The decomposition of PANI presented three stages. The weight loss before 100 °C was caused by the evaporation of moisture absorbed by the film. In the second stage (170-270 °C), the removal of the dopant caused a weight loss of 7.5%. In the third stage (440-590 °C), the thermal weight loss further increased during the decomposition of the polymer skeleton. For ternary composite film BPFP-0.1, a significant three-stage characteristic of PANI decomposition can also be observed, indicating the successful introduction of doped PANI in BPFPs.

The incorporation of insulated Fe_3O_4 reduced the electrical conductivity of composite films (Fig. 5b), and the reduction extent increased with the increasing of Fe_3O_4 loading. However, the electrical conductivity of BPFP-0.1 was comparable to that of BP, around 40 S/cm, due to the contribution by the conductive PANI. The electrical conductivity of the composite film BPP-0.1 was higher than that of the pure carbon nanotube film. This is attributed to the fact that the conductive PANI in the voids between the carbon nanotubes forms conductive bridges, so that the electron transport pathway is more open. In the BP/Fe_3O_4/PANI ternary composite film, the PANI was coated on the surface of the magnetic particles, it played the role of a “bridge” and “binder” between magnetic particles simultaneously (Fig. 5c), as well as between magnetic particles and CNTs, so the ternary composite film had a higher conductivity than the CNT film.

3.3 Magnetic and mechanical properties of composite films

The magnetic properties of Fe_3O_4 and composite films were characterized by VSM at room temperature. The corresponding hysteresis loops are shown in Fig. S4 and Fig. 6a. As shown in Fig. S4, Fe_3O_4-0.01 presented the lowest saturated magnetization (M_s) of 53 emu/g. Then the M_s of Fe_3O_4 increased and reached a plateau (65 emu/g) with the increase of $C_{iron\ ion}$. This could be attributed to the different morphologies of Fe_3O_4 synthesized at different $C_{iron\ ion}$ in Fig. 2. The magnetic properties of granular Fe_3O_4 were superior to those of the needle-like and flaked Fe_3O_4. In terms

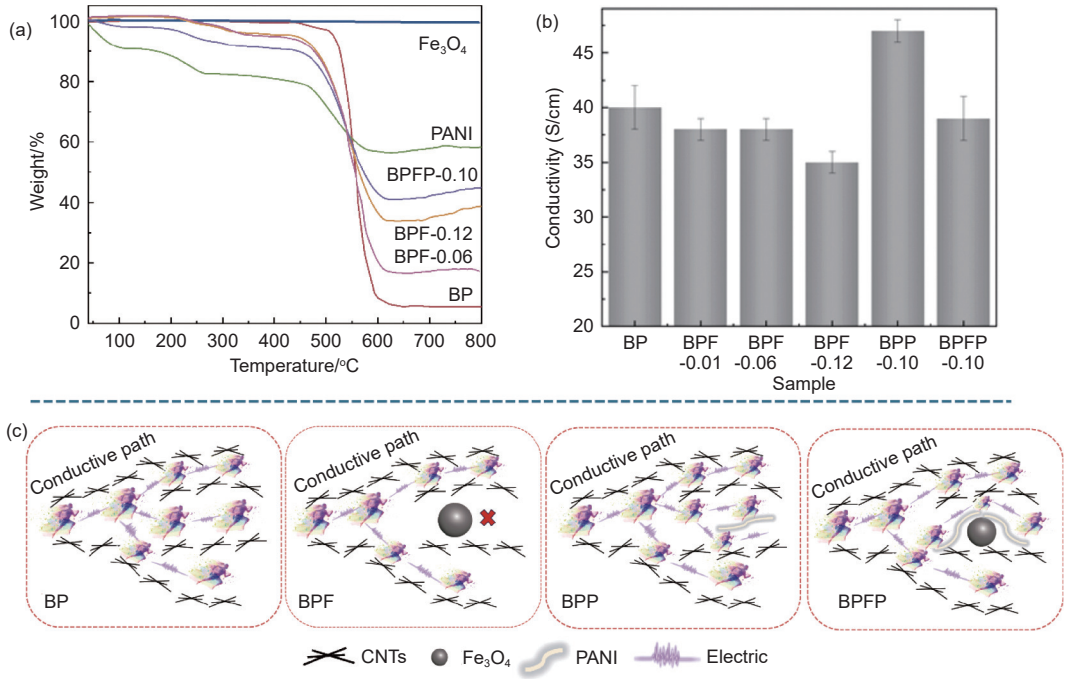

Fig. 5　(a) TGA curves of BP, Fe_3O_4, PANI, and composite films of BP in an oxidative environment. (b) Electrical conductivity of BP and composite films of BP. (c) Schematic diagram of the electric conductive pathway in BP, BPF and BPFP films

of composite films, sample BPF-0.01 presented an M_s of 3.7 emu/g in the presence of Fe_3O_4. The M_s of BPF-0.06 and BPF-0.12 increased to 8.3 and 14.3 emu/g, respectively (Fig. 6a), with the increase of Fe_3O_4 content. The difference between their M_s was not only related to the content of Fe_3O_4, but also related to the M_s of Fe_3O_4 itself. With the combination of PANI, the M_s of BPFP-0.1 decreased slightly (12 emu/g) compared to BPF-0.12 due to the decreased mass fraction of Fe_3O_4. The enhanced M_s of BPF and BPFP improved the eddy current loss and natural resonance loss, which ultimately improved the magnetic loss of these composite films. Besides, the remanence and coercivity for all composite films are listed in Table S1. The magnetic hysteresis loops of composite films were long and narrow, coupled with a small coercive force and remanence, which were the typical characteristics of soft magnetic materials[36]. Furthermore, these composite films maintained the strength (Fig. 6b) and flexibility of BP at the same time. The breaking strength and elongation-at-break of BPFP-0.1 ternary film (14 MPa and 2.1%) were comparable to those of BP.

3.4　Electromagnetic shielding effectiveness of composite films

The EMI *SE* values of BP composite films incorporated with BP, Fe_3O_4 and PANI are shown in Fig. 7a, and EMI SE_A and EMI SE_R are shown in

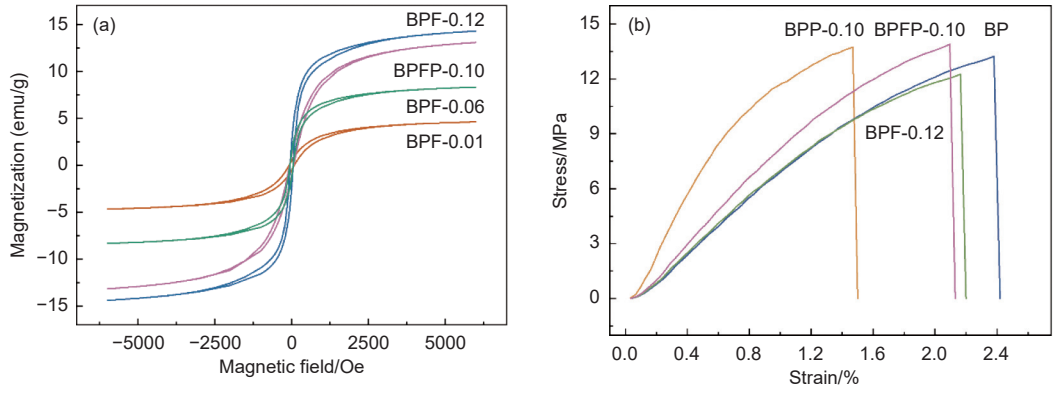

Fig. 6　(a) Magnetic hysteresis curves and (b) stress-strain curves of BPF and BPFP composite films

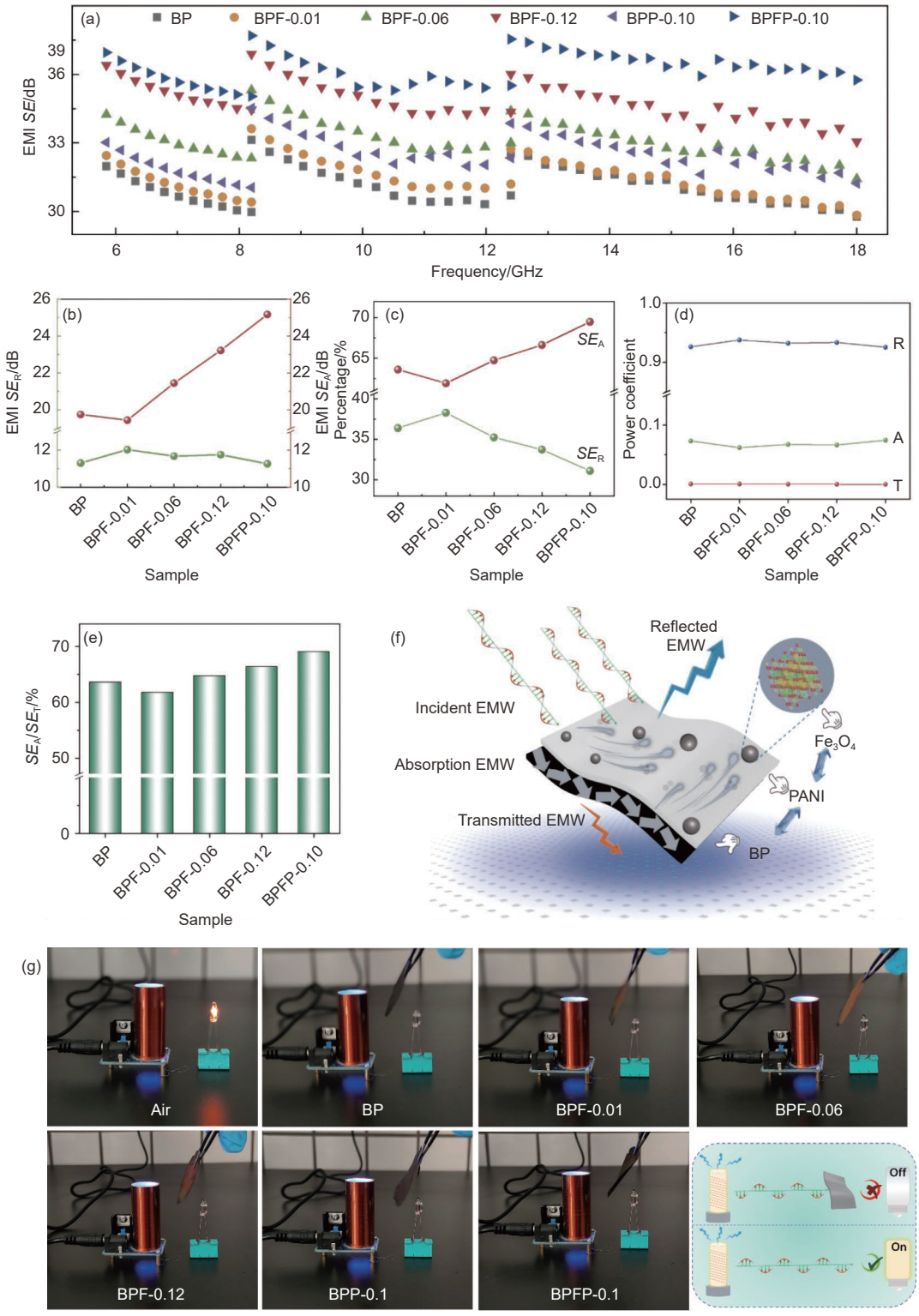

Fig. 7 (a) *SE* values of BP, BPFs, BPP and BPFP over the frequency range of 5.85-18 GHz. (b) The average SE_A and SE_R of BP, BPFs and BPFP. (c) The contribution of SE_A and SE_R to the total *SE*. (d) The average R, A, T of BP, BPFs and BPFP. (e) The average SE_A/SE_T of BP, BPFs and BPFP. (f) EMI *SE* mechanism of BPFP. (g) Shielding effect of BP, BPFs, BPP and BPFP in a Tesla coil and its schematic diagram

Fig. S5. BP with the thickness of only 30 μm presented an average EMI *SE* of 31.1 dB (99.9% attenuation[37]) over the test frequency band. Although the combination of Fe_3O_4 caused a slight decrease in conductivity, the *SE* of BPF-0.06 and BPF-0.12 increased to 33.3 and 35.1 dB, which was improved by

7.1% and 12.9%, respectively, compared to the *SE* of BP. The densely packed Fe_3O_4 nanoparticles on BP developed a heterogeneous environment and also formed strong coupling between each other. Therefore, the magnetic and dielectric losses could be profoundly improved due to interfacial polarizations between Fe_3O_4 and MWCNTs, as confirmed by Raman and XRD results discussed in previous sections. Compared with BPF-0.06, BPF-0.12 showed a higher *SE* due to its larger M_s. In terms of BPFP, the PANI conductive networks acted as bridges between the CNTs and Fe_3O_4 particles, enhancing the interaction between CNTs, Fe_3O_4 and PANI, resulting in elevated interfacial polarizations and dielectric loss. The BPFP-0.1 presented the best shielding performance (36.4 dB) despite its inferior magnetic properties.

To further clarify the shielding mechanism of BP, BPF, and BPFP films, the SE_A and SE_R were analyzed using *S* parameters, including S_{11}, S_{12}, S_{21} and S_{22}. BP had a porous network structure enabling the incident microwaves to be reflected and scattered many times between MWCNT-air interfacial areas until being absorbed[38–39]. Besides, BP exhibited the greater reflection coefficient due to the larger impedance difference between MWCNT-air interfacial areas (Fig. 7d and Fig. S6). Thus, BP with a thickness of 30 μm achieved an SE_A of ~ 19.8 dB and SE_R of ~ 11.3 dB. The contribution of the SE_A (63.7%) was much larger than that of SE_R (36.3%), suggesting an absorption-dominated shielding mechanism of BP.

The SE_A values of BP and BPF-0.12 were found to vary from 19.8 to 23.4 dB with the increasing in Fe_3O_4 content, while the SE_R remained nearly constant. Comparing the SE_A and SE_R of BP, BPFs, and BPFPs (Fig. S5 and Fig. 7b), their differences in *SE*s were mainly caused by SE_A, which was a result of the difference in magnetic properties. In addition, the contribution of SE_A increased with the increasing of Fe_3O_4 content (Fig. 7c and 7e). Furthermore, we tested the EMI shielding effect of BP, BPF, BPP, and BPFP films in a Tesla coil (Fig. 7g). We placed the composite films between a small light bulb and a Tesla coil. The light bulbs on the substrates were all extinguished, which proved that the composite films exhibit exceptional electromagnetic shielding effectiveness. This is because the high loading concentration of Fe_3O_4 enhancing the hysteresis loss, along with the presence of multiple interface scattering between different components, conductive loss, polarization loss and magnetic resonance loss work synergistically, leading to high SE_T and SE_A in the composite film, with a significant amount of electromagnetic waves being dissipated[40–41]. Table 2 exhibits a comprehensive comparison on EMI *SE*/thickness (EMI *SE*/*t*) between this work and recently reported materials. The above results clearly demonstrated that BPFP had

Table 2 A comparison of the EMI *SE*/*t* between this work and recently reported materials

Material	*t*/mm	EMI/dB	*SE*/*t*/(dB/mm)	Ref.
Nylon/graphene nanoplatelet composite papers	0.18	58.1	322.7	[42]
MXene/thermoplastic polyurethane films	0.05	50.7	975.0	[43]
CNT@PDA/EVA composite films	0.08	32.4	405.0	[12]
Layer-by-layer carbon nanotube/boron nitride/rubber composite	1.45	32.5	22.4	[44]
Polyurethane-carbon nanotube composites	0.80	18.1	22.6	[45]
2D $Ti_3C_2T_x$ MXene/polyvinylidene fluoride (PVDF) nanocomposites	1.00	34.5	34.5	[46]
Polymer/graphene@polydopamine composites	0.10	20.0	200.0	[47]
Graphene/SiC-nanowires/ poly(vinylidene fluoride) composites	1.20	32.5	27.1	[48]
Cellulose/MXene nanocomposite paper	0.20	43.0	215.0	[49]
Poly (vinyl alcohol)/transition metal carbide (PVA/MXene) films	0.03	44.4	1644.4	[1]
Ni-embedded hollow porous $Ti_3C_2T_x$ MXene film	0.06	70.7	1285.5	[2]
PVDF/MWCNTs/GO@MWCNTs/AgNWs bilayer structured composite film	0.47	69.1	147.0	[3]
Cellulose reinforced carbon nanotube buckypaper	0.04	24.0	666.9	[4]
Aramid nanofiber/polypyrrole composite films	0.05	35.0	760.9	[50]
BPFP	0.04	36.4	887.8	**This work**

excellent EMI *SE*. Although some MXene-based materials do exhibit superior shielding effectiveness/thickness ratios, the BPFP developed in this study places greater emphasis on application scenarios requiring low cost and easily scalable production.

If the sole goal is to pursue the extreme value of shielding effectiveness per unit thickness, MXene can be introduced for composite modification with CNTs in subsequent studies to construct a CNT/MXene/Fe_3O_4/PANI multi-component synergistic system. This system leverages MXene's advantages of high conductivity and large specific surface area to supply efficient conductive pathways, the 3D network structure of CNTs to maintain material flexibility, and the magnetic loss and interfacial polarization characteristics of Fe_3O_4 and PANI, ultimately achieving the synergistic improvement of shielding effectiveness-to-thickness ratio.

4 Conclusion

Free-standing BPF and BPFP films were prepared by in situ synthesis of Fe_3O_4 on BP and in situ polymerization of aniline on BPF, respectively. The Fe_3O_4 content in BPF films increased from 5% (BPF-0.01) to 35.2% (BPF-0.12) with the increasing of feeding iron-ion concentration, accompanied by morphology change of Fe_3O_4. The M_s values of BPF-0.01, BPF-0.06 and BPF-0.12 were 3.7, 8.3 and 14.3 emu/g, respectively. The incorporation of Fe_3O_4 enhanced both magnetic loss and dielectric loss due to interfacial polarizations between Fe_3O_4 and MWCNTs. Therefore, the average *SE* values of BPF samples in the range of 5.85-18 GHz increased by 1.3% (BPF-0.01, 31.5 dB), 7.1% (BPF-0.06, 33.3 dB) and 12.9% (BPF-0.12, 35.1 dB), respectively, compared with BP (31.1 dB). As for BPFP, the PANI layer served as a protective shell to improve the structural stability of Fe_3O_4 nanoparticles. This gave rise to strengthened interfacial polarization by solid-state charge transfer between MWCNTs, Fe_3O_4 and PANI, thus contributing to the high EMI *SE*. Thus, BPFP-0.1 with a thickness of only 41 μm achieved an average EMI *SE* of 36.4 dB, representing a 17% improvement over that of BP.

References

[1] Jin X, Wang J, Dai L Z, et al. Flame-retardant poly (vinyl alcohol)/MXene multilayered films with outstanding electromagnetic interference shielding and thermal conductive performances[J]. Chemical Engineering Journal, 2020, 380: 122475.

[2] Liu H, Dang J, Lei C, et al. Modulating interface of Ni-Embedded hollow porous $Ti_3C_2T_x$ MXene film toward efficient EMI shielding[J]. Small, 2025: 2410937.

[3] Yang S J, Cao Y, He Y B, et al. A review of the use of graphene-based materials in electromagnetic-shielding[J]. New Carbon Materials, 2024, 39(2): 223-239.

[4] Sumanta S, Rajesh K, Sung S H. Low-value biomass-derived carbon composites for electromagnetic wave absorption and shielding: A review[J]. New Carbon Materials, 2025, 40(2): 293-316.

[5] Li W, Zhu L, Gu J, et al. Microwave absorption properties of fabric coated absorbing material using modified carbonyl iron power[J]. Composites Part B: Engineering, 2011, 42(4): 626-630.

[6] Iijima S. Helical microtubules of graphitic carbon[J]. Nature, 1991, 354(6348): 56-58.

[7] Yang R, Tan Y, Zhou T, et al. A PVDF/MWCNTs/GO@MWCNTs/AgNWs bilayer structured composite film with ultra-high EMI shielding and conductivity performance[J]. Polymer Composites, 2024, 45(12): 11044-11061.

[8] Fan M S, Xia X, Li S, et al. Sustainable bacterial cellulose reinforced carbon nanotube buckypaper and its multifunctionality for electromagnetic interference shielding, Joule heating and humidity sensing[J]. Chemical Engineering Journal, 2022, 441: 136103.

[9] Wu Z P, Liu T, Chen D M, et al. A facile method to improving the electromagnetic interference shielding of a free-standing and foldable carbon nanotube mat[J]. RSC Advances, 2016, 6(67): 62485-62490.

[10] Singh B P, Saket D K, Singh A P, et al. Microwave shielding properties of Co/Ni attached to single walled carbon nanotubes[J]. Journal of Materials Chemistry A, 2015, 3(25): 13203-13209.

[11] Zeng Z, Chen M, Jin H, et al. Thin and flexible multi-walled carbon nanotube/waterborne polyurethane composites with high-performance electromagnetic interference shielding[J]. Carbon, 2016, 96: 768-777.

[12] Wang Z G, Yang Y L, Zheng Z L, et al. Achieving excellent thermally conductive and electromagnetic shielding performance by nondestructive functionalization and oriented arrangement of carbon nanotubes in composite films[J]. Composites Science and Technology, 2020, 194: 108190.

[13] Chaudhary A, Kumar R, Teotia S, et al. Integration of MCMBs/MWCNTs with Fe_3O_4 in a flexible and light weight composite paper for promising EMI shielding applications[J]. Journal of Materials Chemistry C, 2017, 5(2): 322-332.

[14] Yang W, Bai H, Jiang B, et al. Flexible and densified graphene/waterborne polyurethane composite film with thermal conducting property for high performance electromagnetic interference shielding[J]. Nano Research, 2022, 15(11): 9926-9935.

[15] Li Z, Yang W, Zhang C, et al. Multiscale structural design of heterostructured carbon/boron nitride aerogels for efficient thermal conductivity and broadband electromagnetic wave absorption[J]. Chemical Engineering Journal, 2025: 165470.

[16] Feng R, Zhu W, Yang W, et al. Scalable production of flexible and multifunctional graphene-based polymer composite film for high-performance electromagnetic interference shielding[J]. Carbon, 2025, 233: 119875.

[17] Zhu W, Feng R, Li Z, et al. Design strategies and research progress of macrostructure graphene-based electromagnetic shielding materials[J]. Carbon, 2025, 242: 120432.

[18] Biswas S, Arief I, Panja S S, et al. Absorption-dominated electromagnetic wave suppressor derived from ferrite-doped cross-linked graphene framework and conducting carbon[J]. ACS Applied Materials & Interfaces, 2017, 9(3): 3030-3039.

[19] Zheng Y, Wang X, Wei S, et al. Fabrication of porous graphene-Fe_3O_4 hybrid composites with outstanding microwave absorption performance[J]. Composites Part A: Applied Science and Manufacturing, 2017, 95: 237-247.

[20] Wu J, Ye Z, Liu W, et al. The effect of GO loading on electromagnetic wave absorption properties of Fe_3O_4/reduced graphene oxide hybrids[J]. Ceramics International, 2017, 43(16): 13146-13153.

[21] Hou C, Li T, Zhao T, et al. Electromagnetic wave absorbing properties of multi-wall carbon nanotube/Fe_3O_4 hybrid materials[J]. New Carbon Materials, 2013, 28(3): 184-190.

[22] Liu Y, Song D, Wu C, et al. EMI shielding performance of nanocomposites with MWCNTs, nanosized Fe_3O_4 and Fe[J]. Composites Part B: Engineering, 2014, 63: 34-40.

[23] Kumar A, Singh A P, Kumari S, et al. EM shielding effectiveness of Pd-CNT-Cu nanocomposite buckypaper[J]. Journal of Materials Chemistry A, 2015, 3(26): 13986-13993.

[24] Rao B V B, Chengappa M, Kale S N. Lightweight, flexible and thin Fe3O4-loaded, functionalized multi walled carbon nanotube buckypapers for enhanced X-band electromagnetic interference shielding[J]. Materials Research Express, 2017, 4(4): 045012.

[25] Lu S, Xu W, Xuhai X, et al. Preparation, magnetism and microwave absorption performance of ultra-thin Fe_3O_4/carbon nanotube sandwich buckypaper[J]. Journal of Alloys and Compounds, 2014, 606: 171-176.

[26] Hu Y P, Li D C, Wu L, et al. Carbon nanotube buckypaper and buckypaper/polypropylene composites for high shielding effectiveness and absorption-dominated shielding material[J]. Composites Science and Technology, 2019, 181: 107699.

[27] Hu Y P, Li D C, Tang P, et al. Comparative study of structure, mechanical and electromagnetic interference shielding properties of carbon nanotube buckypapers prepared by different dispersion media[J]. Materials & Design, 2019, 184: 108175.

[28] Arjmand M, Apperley T, Okoniewski M, et al. Comparative study of electromagnetic interference shielding properties of injection molded versus compression molded multi-walled carbon nanotube/polystyrene composites[J]. Carbon, 2012, 50(14): 5126-5134.

[29] Song W L, Guan X T, Fan L Z, et al. Tuning three-dimensional textures with graphene aerogels for ultra-light flexible graphene/texture composites of effective electromagnetic shielding[J]. Carbon, 2015, 93: 151-160.

[30] Singh K, Ohlan A, Kotnala R K, et al. Dielectric and magnetic properties of conducting ferromagnetic composite of polyaniline with γ-Fe_2O_3 nanoparticles[J]. Materials Chemistry and Physics, 2008, 112(2): 651-658.

[31] Diez-Pascual A M, Gascon D. Carbon nanotube buckypaper reinforced acrylonitrile–butadiene–styrene composites for electronic applications[J]. ACS Applied Materials & Interfaces, 2013, 5(22): 12107-12119.

[32] Subrahmanyam K S, Manna A K, Pati S K, et al. A study of graphene decorated with metal nanoparticles[J]. Chemical Physics Letters, 2010, 497(1-3): 70-75.

[33] Kitaura R, Imazu N, Kobayashi K, et al. Fabrication of metal nanowires in carbon nanotubes via versatile nano-template reaction[J]. Nano Letters, 2008, 8(2): 693-699.

[34] Wang W, Wang K, Wang R, et al. Synthesis of Fe-filled thin-walled carbon nanotubes with high filling ratio by using dichlorobenzene as precursor[J]. Carbon, 2007, 45(5): 1127-1129.

[35] Li J, Tang S, Lu L, et al. Preparation of nanocomposites of metals, metal oxides, and carbon nanotubes via self-assembly[J]. Journal of the American Chemical Society, 2007, 129(30): 9401-9409.

[36] Bao Y, Li J, Wang T, et al. Photothermal programming of magnetic soft materials for complex and reconfigurable 3D deformations[J]. Science China Materials, 2024, 67(12): 4031-4039.

[37] Yan D X, Pang H, Li B, et al. Structured reduced graphene oxide/polymer composites for ultra-efficient electromagnetic interference shielding[J]. Advanced Functional Materials, 2015, 25(4): 559-566.

[38] Wang H, Zheng K, Zhang X, et al. 3D network porous polymeric composites with outstanding electromagnetic interference shielding[J]. Composites Science and Technology, 2016, 125: 22-29.

[39] Wang J, Xiang C, Liu Q, et al. Ordered mesoporous carbon/fused silica composites[J]. Advanced Functional Materials, 2008, 18(19): 2995-3002.

[40] Li H, Bi S, Cai J, et al. Reduced graphene oxide/nonwoven fabric filled honeycomb composite structure for broadband microwave absorption[J]. Carbon, 2024, 223: 119005.

[41] Bi S, Song Y Z, Hou G L, et al. Sandwich nanoarchitectonics of heterogenous CB/CNTs honeycomb composite for impedance matching design and microwave absorption[J]. Journal of Alloys and Compounds, 2023, 943: 169154.

[42] Wang W, Ma X, Shao Y, et al. Flexible, multifunctional, and thermally conductive nylon/graphene nanoplatelet composite papers with excellent EMI shielding performance, improved hydrophobicity and flame resistance[J]. Journal of Materials Chemistry A, 2021, 9(8): 5033-5044.

[43] Gao Q, Pan Y, Zheng G, et al. Flexible multilayered MXene/thermoplastic polyurethane films with excellent electromagnetic interference shielding, thermal conductivity, and management performances[J]. Advanced Composites and Hybrid Materials, 2021, 4: 274-285.

[44] Zhan Y, Lago E, Santillo C, et al. An anisotropic layer-by-layer carbon nanotube/boron nitride/rubber composite and its application in electromagnetic shielding[J]. Nanoscale, 2020, 12(14): 7782-7791.

[45] Shin B, Mondal S, Lee M, et al. Flexible thermoplastic polyurethane-carbon nanotube composites for electromagnetic interference shielding and thermal management[J]. Chemical Engineering Journal, 2021, 418: 129282.

[46] Cheng H, Pan Y, Chen Q, et al. Ultrathin flexible poly (vinylidene fluoride)/MXene/silver nanowire film with outstanding specific EMI shielding and high heat dissipation[J]. Advanced Composites and Hybrid Materials, 2021, 4: 505-513.

[47] Wei L, Ma J, Zhang W, et al. pH triggered hydrogen bonding for preparing mechanically strong, electromagnetic interference shielding and thermally conductive waterborne polymer/graphene@polydopamine composites[J]. Carbon, 2021, 181: 212-224.

[48] Liang C, Hamidinejad M, Ma L, et al. Lightweight and flexible graphene/SiC-nanowires/poly (vinylidene fluoride) composites for electromagnetic interference shielding and thermal management[J]. Carbon, 2020, 156: 58-66.

[49] Hu D, Huang X, Li S, et al. Flexible and durable cellulose/MXene nanocomposite paper for efficient electromagnetic interference shielding[J]. Composites Science and Technology, 2020, 188: 107995.

[50] Guo D, Mu C, Liu Q, et al. Aramid nanofiber/polypyrrole composite films for broadband EMI shielding, wearable electronics, Joule heating, and photothermal conversion[J]. ACS Applied Nano Materials, 2023, 6(16): 15108-15118.